

Automatic identification of fault zone head waves and direct P waves and its application in the Parkfield section of the San Andreas Fault, California

Zefeng Li and Zhigang Peng

School of Earth and Atmospheric Sciences, Georgia Institute of Technology, Atlanta, GA, USA. E-mail: zli354@gatech.edu

Accepted 2016 February 26. Received 2016 February 18; in original form 2015 December 18

SUMMARY

Fault zone head waves (FZHWs) are observed along major strike-slip faults and can provide high-resolution imaging of fault interface properties at seismogenic depth. In this paper, we present a new method to automatically detect FZHWs and pick direct P waves secondary arrivals (DWSAs). The algorithm identifies FZHWs by computing the amplitude ratios between the potential FZHWs and DSWAs. The polarities, polarizations and characteristic periods of FZHWs and DSWAs are then used to refine the picks or evaluate the pick quality. We apply the method to the Parkfield section of the San Andreas Fault where FZHWs have been identified before by manual picks. We compare results from automatically and manually picked arrivals and find general agreement between them. The obtained velocity contrast at Parkfield is generally 5–10 per cent near Middle Mountain while it decreases below 5 per cent near Gold Hill. We also find many FZHWs recorded by the stations within 1 km of the background seismicity (i.e. the Southwest Fracture Zone) that have not been reported before. These FZHWs could be generated within a relatively wide low velocity zone sandwiched between the fast Salinian block on the southwest side and the slow Franciscan Mélange on the northeast side. Station FROB on the southwest (fast) side also recorded a small portion of weak precursory signals before sharp P waves. However, the polarities of weak signals are consistent with the right-lateral strike-slip mechanisms, suggesting that they are unlikely genuine FZHW signals.

Key words: Earthquake dynamics; Body waves; Guided waves; Rheology and friction of fault zones.

1 INTRODUCTION

Large mature strike-slip faults tend to juxtapose blocks with clear lithological contrast (e.g. Thurber *et al.* 2006; Wdowinski *et al.* 2007; Dor *et al.* 2008). The resulting velocity contrast leads to significant differences in rupture behaviour and seismic radiation from a homogeneous solid (Ben-Zion 2001). For a mode-II type rupture, the dynamic change of normal stress σ_n at the rupture tip along a bimaterial interface is opposite in two slip directions: the change of σ_n is tensile along the slip direction of the compliant solid, and compressive along the other direction (Weertman 1980; Andrews & Ben-Zion 1997; Shi & Ben-Zion 2006). This dynamic effect may result in a statistically preferred rupture direction when an earthquake initiates within a bimaterial interface (Brietzke & Ben-Zion 2006; Dalguer & Day 2009; Ampuero & Ben-Zion 2008). Because of drastic difference in the resulting ground motion due to directivity effect, a better understanding of bimaterial fault interface properties is important for seismic hazard assessment (e.g. Ben-Zion 2006; Brietzke *et al.* 2009; Xu *et al.* 2012).

Bimaterial fault interface is expected to generate fault zone head waves (FZHWs), which refract along the interface with the

seismic velocity of the fast side and radiate from the fault to the slow side (Ben-Zion 1989, 1990). Beyond a critical distance, FZHWs arrive earlier than direct P waves at stations on the slow side. In such cases, direct P waves can be termed as direct wave secondary arrival (DWSA; Ben-Zion & Malin 1991; Bennington *et al.* 2013). The arrival time differences between the FZHWs and DWSAs can be used to estimate velocity contrast along a fault interface (Ben-Zion *et al.* 1992; Zhao *et al.* 2010; Allam *et al.* 2014). In addition, incorporating FZHWs into traveltimes tomography produces a sharper velocity contrast across the Parkfield section of the San Andreas Fault (SAF) than using the direct arrivals alone (Bennington *et al.* 2013). Furthermore, distinguishing preceding FZHWs from direct P arrivals can enhance the accuracy of focal mechanism and event location (Ben-Zion & Malin 1991).

To obtain a robust estimate of velocity contrast along a fault, typically we need a large number of FZHWs and DWSAs. In most previous studies, FZHWs and DWSAs are picked manually, which is an onerous task. More importantly, visual identifications of these phases depend on personal experience and therefore are subjective. In addition, for quality control purpose, Zhao *et al.* (2010) classified the picks of FZHWs into three quality levels in terms of the

sharpness of amplitude changes, which is again based on visual inspection. Recently, Ross and Ben-Zion (2014) developed a new algorithm for automatic picking of direct P , S phases and FZHWs. They first picked the initial phases by short-term-average/long-term-average (STA/LTA) ratio function. Next, they distinguished between FZHWs and DWSAs by calculating kurtosis and skewness functions, which are sensitive to polarity changes and other abrupt changes in waveform characteristics. In their algorithm, the arrival differences between FZHWs and DWSAs are upper bounded by the prediction of the maximum velocity contrast in the given region.

In this paper, we present an alternative method to automatically distinguish between FZHWs and DWSAs based primarily on their amplitude differences and other characteristics. Different from the algorithm in Ross & Ben-Zion (2014), our method is based on pre-existing first phase arrivals, and evaluates if the first arrival is a potential FZHW or simply a direct P wave. If it is a FZHW, our algorithm will pick the P wave or DSWA. To do this, we define new metrics of long-term and short-term amplitude ratios to track amplitude change. In addition, we propose a set of criteria for quality control purpose. The method is designed to fully exploit the characteristics of FZHWs and DWSAs, including amplitude, polarity, frequency, and polarization difference.

In the following sections, we first describe the method and various quality control parameters. Next, we apply our method to the Parkfield section of the SAF, where Zhao *et al.* (2010) have previously analysed FZHWs and found clear variation of velocity contrast along the SAF strike. We systematically compare our results with manual picks by Zhao *et al.* (2010) and re-calculate the velocity contrast using the automatic picks.

2 METHOD

FZHWs are identified as emergent first arrivals and low-amplitude seismic signals with lower frequency and opposite polarities with respect to the direct P waves (e.g. Ben-Zion & Malin 1991; McGuire & Ben-Zion 2005). In addition, P waves are expected to polarize along the source-receiver direction while FZHWs are polarized in a direction controlled by the percentage of velocity contrast and local fault geometry (Bulut *et al.* 2012). Our automatic phase picking algorithm is based primarily on amplitude and polarity differences between these two phases. Other characteristics are used as additional quality control factors. The flow chart of the entire process is shown in Fig. 1, with each step illustrated below.

2.1 Basic quantities

The velocity contrast across the bimaterial interface can be described by the degree K :

$$K = \frac{V_f - V_s}{V} \approx \frac{t_p - t_{hw}}{t_p - t_0} \approx \frac{t_p - t_{hw}}{t_{hw} - t_0}, \quad (1)$$

where V_f , V_s and V denote the velocities of the fast side, slow side and the average, respectively. t_p , t_{hw} and t_0 are the traveltimes of the DWSA and FZHW, and event origin time, respectively.

The approximation made in eq. (1) allows us to determine the search range for DWSA without assuming absolute velocities of both sides of the fault. If the event origin time t_0 and first arrival t_1 (either direct P waves or FZHWs) are known, the maximum search range t_2 for potential DWSA can be set by

$$t_2 = t_1 + K_{\max} (t_1 - t_0), \quad (2)$$

where K_{\max} is the maximum degree of velocity contrast allowed in a region. In this study we set $K_{\max} = 15$ per cent for the Parkfield case, above the maximum value of 10 per cent observed by Zhao *et al.* (2010), and the maximum value of 10 per cent used in Ross & Ben-Zion (2014).

Another important parameter used in the algorithm is the dominant period of the examined waveform. When the examined window is generally very short (typically less than 0.5 s), especially less than a full cycle of the dominant waveform, Fourier transform usually produces artefacts in the spectra domain due to window edge effect (Peng *et al.* 2011). Therefore, instead of Fourier spectrum, we use median instantaneous dominant frequency following the definition by Barnes (1993), which is found to be more stable for very short time window. Instantaneous dominant frequency $f_d(t)$ can be calculated from instantaneous frequency $f_i(t)$, the instantaneous amplitude or envelope $E(t)$ and its time derivative $E'(t)$ as

$$f_d^2(t) = f_i^2(t) + \left(\frac{E'(t)}{2\pi E(t)} \right)^2. \quad (3)$$

The median value of the instantaneous dominant frequency trace is taken to be a counterpart of spectral dominant frequency. The dominant period T_d is reciprocal of f_d , and bounded within [0.05, 0.2] s. We use this quantity to approximate one full cycle of the early arriving waveforms.

2.2 Search parameters

To check if an initial arrival is a potential FZHW or direct P waves, the first characteristic is the sharpness of the first arrival. A FZHW generally has low amplitude and is followed by an abrupt increase of DWSA (Ben-Zion & Malin 1991). Typically we pick its onset at a place with a sharp increase of amplitude in the displacement seismogram (Ben-Zion 1989; Zhao *et al.* 2010). In practice, we can evaluate the amplitude change within a short segment of waveforms and compare the amplitude over a relative long window. To mimic this process, we use quantities that are named as long-term and short-term average amplitude ratios.

We define long-term average amplitude ratio (LAAR) and short-term average amplitude ratio (SAAR) by

$$\text{LAAR}(t) = \frac{\int_t^{t_2} A^2(\tau) d\tau}{t_2 - t} \bigg/ \frac{\int_{t_1}^t A^2(\tau) d\tau}{t_p - t_1} \cdot R^\alpha(t), \quad t \in [t_1 + T_d, t_2 - T_d] \quad (4)$$

$$\text{SAAR}(t) = \int_t^{t+T_d} A^2(\tau) d\tau \bigg/ \int_{t-T_d}^t A^2(\tau) d\tau \cdot R^\alpha(t), \quad t \in [t_1 + T_d, t_2 - T_d] \quad (5)$$

$$R(t) = \int_t^{t+T_d} A^2(\tau) d\tau \bigg/ \int_{t_1}^{t_1+T_d} A^2(\tau) d\tau, \quad (6)$$

where $A(t)$ is the amplitude at t , and $R(t)$ is the amplitude ratio between the window right after t and the initial window. α is a small constant to modulate the effect of $R(t)$. LAAR consists of the global-sense amplitude change weighted by $R(t)$, while SAAR consists of the local-sense amplitude change weighted by $R(t)$ as well. We add the term $R(t)$ because we find that without this term, LAAR and SAAR are sensitive to low-amplitude signal prior to real FZHW arrivals. Because we rely on the first arrival picks by other methods, and the first arrival may be sometimes picked slightly early than the

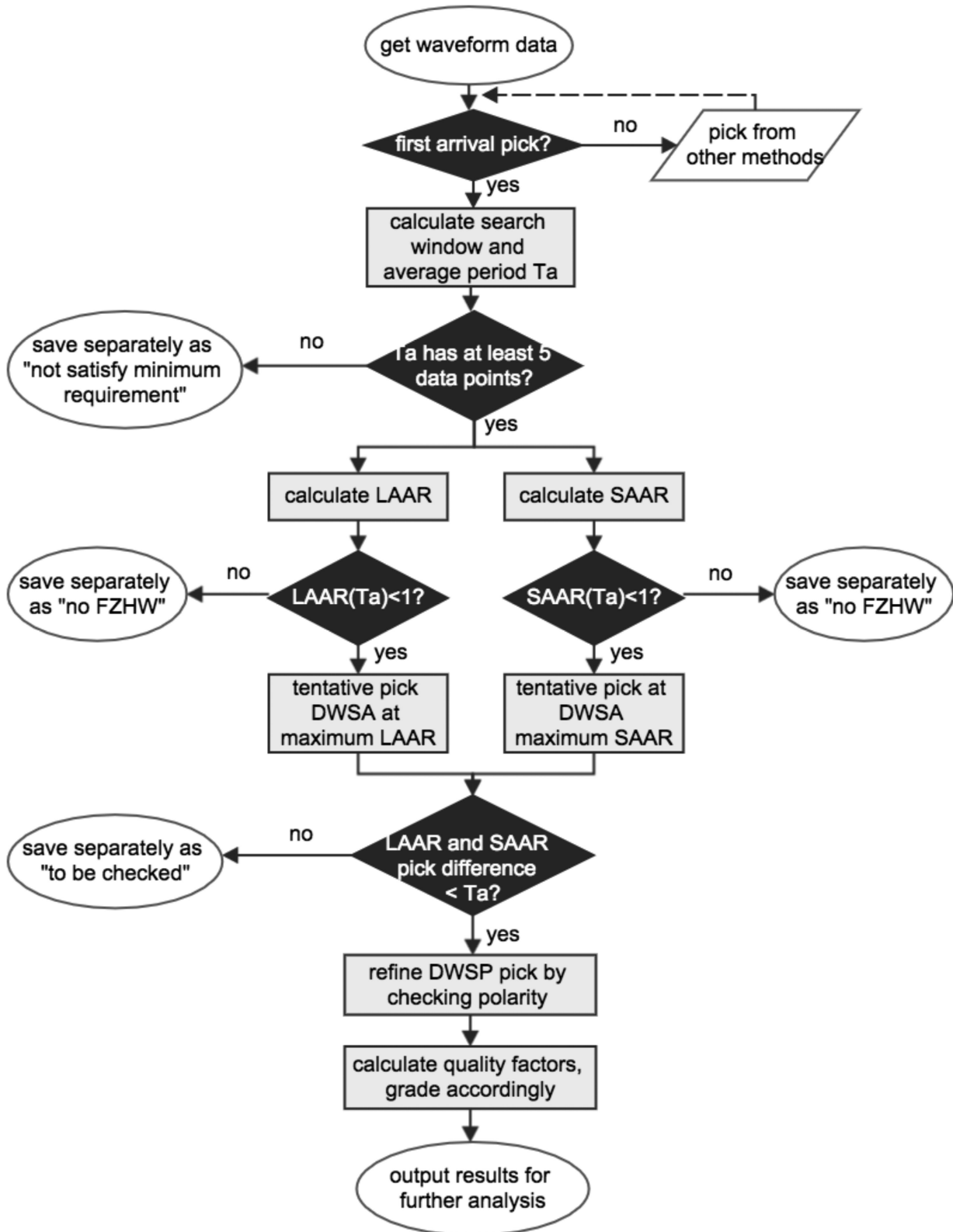


Figure 1. A flow chart of the algorithm for automatic detection of fault zone head waves (FZHW) and picking direct wave secondary arrival (DWSA) (i.e. the direct P wave). LAAR: long-term average amplitude ratio; SAAR: short-term average amplitude ratio.

real arrival. Therefore, the examined window contains a section of noise at the very beginning, and without the term $R(t)$ LAAR and SAAR will erroneously pick at the first arrival. Including the term $R(t)$ can inhibit such error and helps to pick at position with more

significant large amplitude. α is to fine-tune the effect of $R(t)$ and cannot be too large to override other terms. In this study we set α to be a small constant 0.1. An example demonstrating the functionality of $R(t)$ is shown in Supporting Information Fig. S1. Although the

Table 1. Quality criteria.

Quality	Criteria for three-component measurement	Criteria for vertical component measurement
A	Satisfy polarity, period and polarization requirements. Peak LAAR and SAAR have the significant level greater five times standard deviation.	Satisfy polarity and period requirements. Peak LAAR and SAAR have the significant level greater five times standard deviation.
B	Not in A quality, but satisfy two of polarity, period and polarization requirements.	Not in A quality, but satisfy one of polarity and period requirements.
C	Not in A or B quality, but satisfy one of polarity, period and polarization requirements.	

$\alpha = 0.1$ is somewhat subjective, we find that a small change around 0.1 does not change the results significantly.

Next we use the parameters LAAR and SAAR to judge whether the initial pick is a potential FZHW or simply a sharp direct wave. If LAAR or SAAR at $t_1 + T_d$ is less than one, the amplitude within the first T_d is larger than the remaining waveform portion. This indicates that the initial phase has large amplitude and is sharp, and thus considered as a direct wave. Otherwise, the first arrival is treated as a potential FZHW. In this case, the second task is to pick DWSA. To do this, we take the times corresponding to the maximum of LAAR and SAAR within the search window as two tentative picks of DWSA. If the difference of these two picks is small enough, these picks are considered to be consistent in both ‘global’ and ‘local’ senses, which intuitively mimics manual picking consideration. The upper limit of the time difference is taken as T_d .

Next, the tentative pick of the DWSA is set to be the average times corresponding to the maximum LAAR and SAAR values. Since the polarities of FZHWs and DWSAs are opposite for a strike-slip focal mechanism and vertical faulting, we also check the polarity at the average time. If the corresponding polarity is opposite to that of the FZHW, this is set to be the final pick time. Otherwise, we search for a peak, trough or zero-crossing with opposite polarity within a window of T_d length centred at the average pick. If such position exists, the pick will be revised to the nearest one. Otherwise, the pick will remain at the average pick, but tagged with one that does not satisfy the polarity requirement. Note that due to the existence of noise, it is generally unstable to check polarity of FZHWs using the peaks or troughs around early portion of initial phase (Ross & Ben-Zion 2014). Therefore, we check the polarity of the first phase by averaging the amplitude over a $T_d/4$ window after t_1 and comparing it with the value at t_1 .

2.3 Quality control

Zhao *et al.* (2010) evaluated the picking quality by visually inspecting the sharpness of amplitude change. To mimic this in a more objective way, we use the following five criteria to judge the resulting quality of DWSA picks. These include polarity, period and polarization, and values of LAAR and SAAR at the final picks. As mentioned before, the polarity of DWSA is expected to be opposite to that of FZHW and thus can be used as the first quality factor. Second, FZHWs usually have longer periods than direct P waves (Ben-Zion & Malin 1991). The periods of FZHW and DWSA are estimated within their respective windows using the same algorithm of T_d calculation ($t_1 - t_p$ for FZHW and $t_p - t_2$ for DWSA). We expect that the average period T_d for FZHW to be larger than that of DWSA. Third, FZHWs are polarized in a direction deviated from the source-receiver direction, and thus horizontal polarization can

be used to help identify FZHWs (Bulut *et al.* 2012; Yang *et al.* 2015).

The polarization angles of FZHWs and P waves are computed using a covariance matrix method (Jurkevic 1988). Here we focus on horizontal polarization and thereby use a 2-D covariance matrix

$$\sigma = \begin{bmatrix} \text{Cov}(N, N) & \text{Cov}(N, E) \\ \text{Cov}(E, N) & \text{Cov}(E, E) \end{bmatrix}, \quad (7)$$

where N and E are North and East components, respectively. Assuming that the covariance matrix has two eigenvalues $\lambda_1 \geq \lambda_2$, the corresponding eigenvectors are u_1 and u_2 , where the primary polarization angle is along the direction of u_1 . The FZHW and DWSA window are taken as $0.8 \times (t_p - t_{hw})$ following the FZHW and DWSA arrivals to calculate their respective covariance matrixes. For ideal FZHW and DWSA, the polarization angle is expected to meet

$$|\phi_{hw} - \phi_0| > |\phi_p - \phi_0|, \quad (8)$$

where ϕ_{hw} and ϕ_p are the polarization angles of FZHW and DWSA, and ϕ_0 is the back azimuth.

We evaluate the quality of FZHWs by the number of parameters satisfying pre-defined criteria, along with significant level of amplitude changes (Table 1). For measurements with three components, quality ‘A’ means that the measurements satisfy all three requirements: polarity, period and polarization. Besides, peak LAAR and SAAR values at the final picks should be five times standard deviation above the average value. Although somewhat subjective, we find this threshold readily indicative of an abrupt amplitude change from FZHW to DWSA. Measurements that meet two requirements and have regular amplitude change are classified as ‘B’. Measurements only satisfying one requirement have quality ‘C’. The measurements satisfy none of the above criteria are discarded. For the measurements with only vertical components, we follow a similar grading scheme, with a difference that horizontal polarization is excluded (Table 1).

3 PARKFIELD DATA

We apply the method to seismic data around the Parkfield section of the SAF, where Zhao *et al.* (2010) have manual picked FZHWs and DWSAs and found clear along-strike variations of velocity contrast (Fig. 2). We use the same seismic data from the borehole High Resolution Seismic Network (HRSN) in 2001–2005, the temporary Parkfield Area Seismic Observatory (PASO) in 2001–2002 and the surface permanent North California Seismic Network (NCSN) in 1984–2005.

The pre-processing steps basically follow Zhao *et al.* (2010), and are briefly described here. We first select events that are confined within 1 km from the fault interface (approximated by a line with

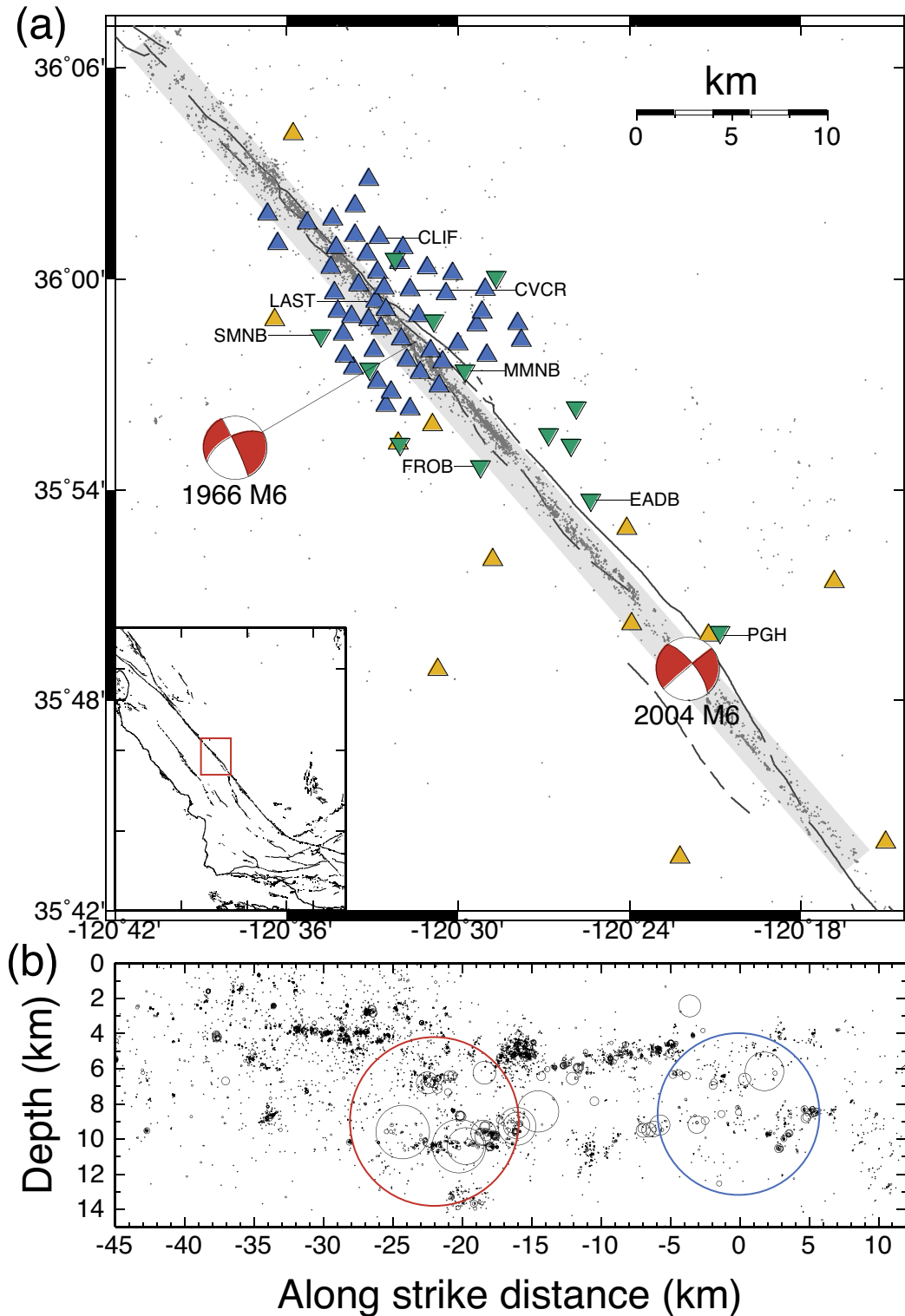


Figure 2. (a) A map of the Parkfield section of the San Andreas Fault. Blue and yellow triangles are surface station in the PASO and NCSN, respectively. Green inverse triangles are borehole stations in the HRSN. Selected station names are labelled. Two beach balls represent the focal mechanisms of the 1966 and 2004 M6-type Parkfield earthquakes. The background seismicity from 1984–2005 (Thurber *et al.* 2006) are marked with dots. The light grey boxes mark the region (along-strike distance: -15 to 45 km, fault-perpendicular distance: -1 to 1 km) where events are used in this study and stations are considered as the FZ group. The inset shows the active faults in California and the red box marks our study area. (b) Hypocenters of seismicity from 1984–2005. The red and blue circles mark the 1966 and 2004 M6-type earthquakes, respectively. The radii of the circles are estimated from its magnitude by assuming a nominal 3-MPa stress drop. After Zhao *et al.* (2010).

139.2° clockwise from north passing through 120.366 W 35.815 N, the epicentre of the 2004 M6 Parkfield earthquake). Next we remove the mean value of each velocity seismogram and apply a 1 Hz high pass filter to the data, and select high-quality waveforms with signal-to-noise ratio (SNR) > 5 for the HRSN data and SNR > 10 for the PASO and NCSN data. The PASO data is recorded by three components while the most NCSN data is recorded on vertical component only. Although HRSN data is recorded by three components, the horizontal orientations are not well constrained (T. Taira, personal communication, 2011). Hence, we use the vertical component only for stations in the NCSN and HRSN.

Next, we select station-event pairs which manual phase picks (either *P* wave only, or with both FZHWs and DWSAs) by Zhao *et al.* (2010). The resulting data consists of 31 648 waveforms from HRSN, 6386 from PASO, and 3393 from NCSN. Among these waveforms, there are 6271, 805 and 277 manual FZHW picks in the HRSN, PASO and NCSN data, respectively. We use the first arrival picks by Zhao *et al.* (2010) as an input, which also enable us to make a direct comparison with their results.

We divide the stations into three groups according to their relative locations to the fault. The fault-zone (FZ) group consists of stations that are located less than 1 km within the fault surface trace (approximated by a straight line same as the one for event selection). The remaining stations are classified as NE or SW groups relative to the fault. As a result, there are 16, 36 and 22 stations belonging to the FZ, NE and SW groups, respectively.

4 RESULTS

4.1 General patterns

Overall we obtain 4612 automatic DWSA picks in HRSN, 973 in PASO and 262 in NCSN, which are comparable with manual picked arrivals (6271, 805 and 277 in HRSN, PASO and NCSN). Fig. 3 shows the percentage of identified FZHWs among the first arrivals on each station. Overall, the NE and FZ stations have 19.0 per cent and 19.3 per cent events that produce FZHWs, respectively. Some stations (e.g. the PASO station LAST and the HRSN station SCYB) have FZHW observations higher than 40 per cent. In comparison, the SW stations have only 4.7 per cent and most SW stations have few or no FZHW recordings. The only exception is the FROB station, which has 18.5 per cent of FZHW observation. Fig. 4 shows pick examples on three-component data for quality grade A, B and C (Figs 4a–c), and A, B for vertical-component only (Figs 4c and d). In general, qualities A, B and C correspond excellent, good and fair picks, respectively. And as shown below, higher quality picks show generally better consistency with manual picks.

4.2 Comparison with manual picks

In this section we compare the automatic and manual picks for all analysed events. Figs 5(a) and (b) show the time differences between DWSAs and FZHWs between the automatically and manually picked phases. Although with some scatters, the majority of them cluster near the 1:1 line. The histogram (Fig. 5c) of residuals between automatic and manual picks is concentrated around zero, and 60 per cent of them are within 0.03 s, that is, three data samples. The mean residual is -0.01 s, suggesting a minimal systematic picking difference between the manual and automatic picks. The relative pick difference, which is defined as the difference over their mean, shows a relative wide spread (Fig. 5d). Although some

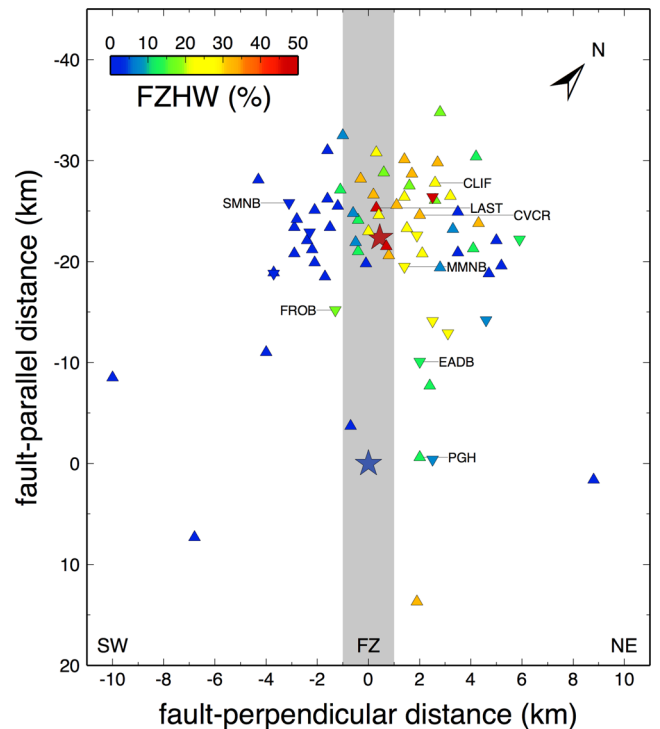


Figure 3. Percentage of FZHW observation on each station from the automatic detection. We rotate the station coordinate into fault-parallel (139.2° clockwise from north) and fault-perpendicular direction. Triangles and inverse triangles are surface and borehole stations, respectively. Selected stations are labelled. The percentage of FZHW observation at each station is colour coded. Note that the stations on the SW (fast) side generally have a very small percentage of FZHW observation. The red and blue stars mark the epicentres of the 1966 and 2004 M6-type Parkfield earthquakes, respectively. The grey shaded area marks the ± 1 km around the majority of seismicity and approximate low-velocity zone.

of the automatic picks change by more than 100 per cent, most of them are concentrated within 25 per cent of change. In addition, Fig. 6 shows comparisons between automatic and manual picks in different quality grades. Generally automatic picks with higher qualities are more consistent with manual picks, which reflects their quality grades to certain extents.

If the bimaterial interface is coherent along the interface, the differences of DWSA and FZHW are expected to systematically increase with fault interface distance (Ben-Zion & Malin 1991). Hence the average velocity contrast can be estimated the following equation:

$$dt \sim r \left(\frac{1}{V_s} - \frac{1}{V_f} \right) \sim r \left(\frac{V_f - V_s}{V^2} \right) \quad (9)$$

where dt is arrival difference between DWSA and FZHW, r is along-interface distance and V is the average velocity which is assumed to be 5.5 km s^{-1} in this region (Zhao *et al.* 2010). Here we obtain the slope and its uncertainty using linear regression without the intercept term, which is slightly different from Zhao *et al.* (2010). We exclude the intercept term because it has no clear physical meaning according to eq. (9). In other words, we force arrival time difference dt to be zero with zero along-strike distance.

Next we calculate velocity contrast on the stations that have at least 50 input waveforms and the FZHW percentage higher than 10 per cent. For comparison, we also recalculate the velocity contrast from the manual picks of Zhao *et al.* (2010) using the

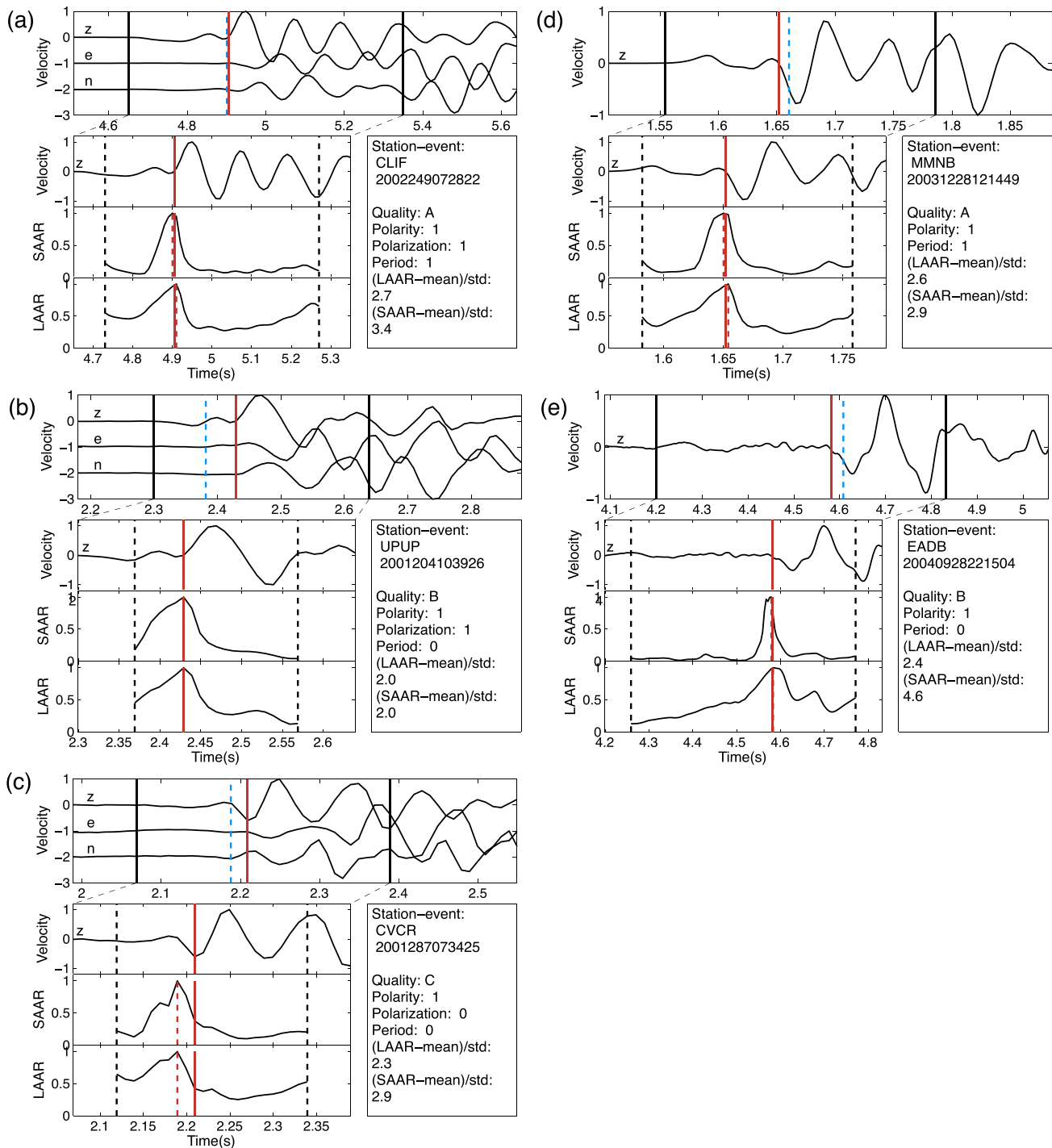


Figure 4. Pick examples with different qualities for measurements on three components at the PASO stations. (a) An example of quality A picks on three components at station CLIF. The top panel is normalized three-component velocity seismogram. The left and right solid black vertical bars mark the first arrival and the end of search window. The left and right dashed black vertical bars mark one average period length that is used as minimal window of FZHW and DWSA when calculating LAAR and SAAR, respectively. The red bar marks the final pick. Note that red and blue bars may overlap. The left bottom three panels are the vertical waveform, LAAR, and SAAR curve within the search window. The blue bars mark the tentative pick at the LAAR or SAAR maximum, and the red bar marks the final pick. The information and quality factors are listed in the right panel. Panels (b) and (c) are examples for B and C qualities using three-component grade scheme, respectively. The symbols are the same as in panel (a). Panels (d) and (e) are examples of A, B qualities for vertical-component grade scheme, respectively.

fitting function without intercept term (eq. 9). Fig. 7 shows examples of FZHWs at the PASO station CLIF and the HRSN station EADB using automatic and manual DWSA picks, respectively. At station CLIF, velocity contrasts at the NW side measured from

automatic and manual picks are ~ 9 per cent, although the difference at the SE side is slightly greater than 1 per cent. The velocity contrasts at station EADB for events at both the NW and SE side are consistent.

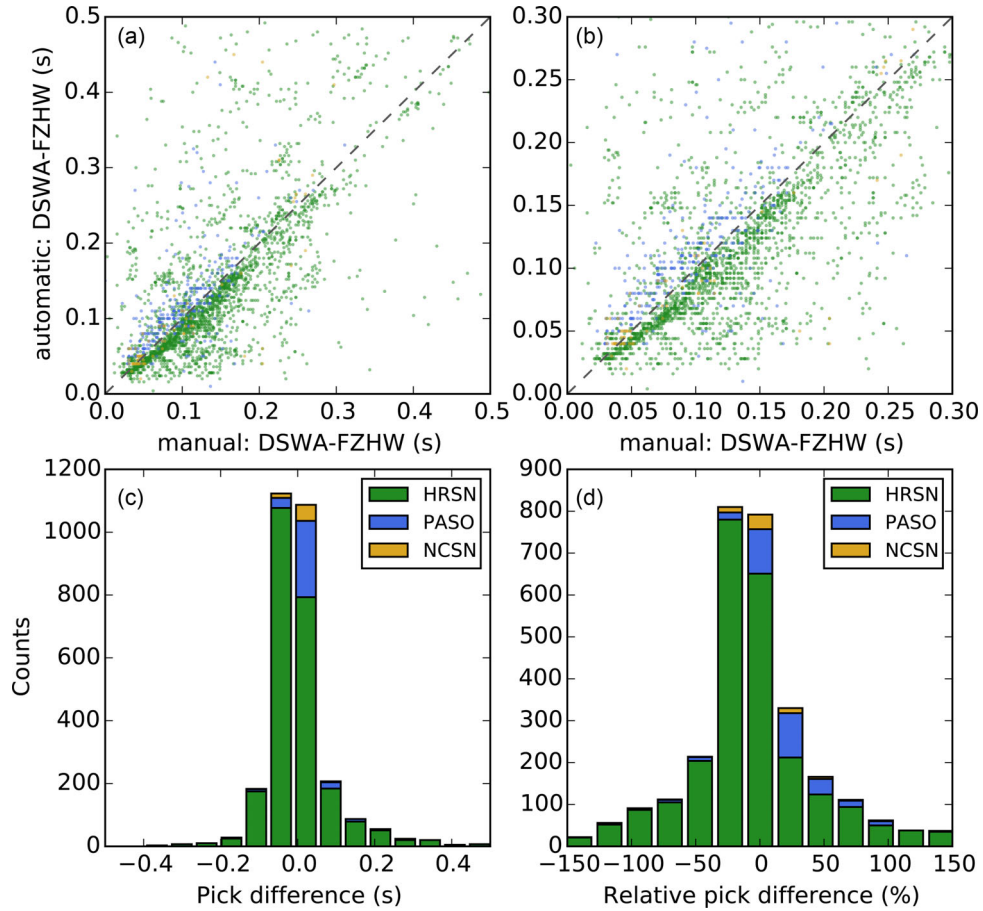


Figure 5. Comparison between automatically and manually picked time differences between the DWSAs and FZHWs. (a) Green, blue and yellow dots represent the time differences between DWSA and FZHW picks on HRSN, PASO and NCSN, respectively. The thick black line is the one to one line. (b) A zoom-in plot of panel (a) in the 0–0.3 s window. (c) Histogram of the automatically and manually picked time differences with 0.05 s bin width. Green, blue and yellow bars mark the results for the HRSN, PASO and NCSN, respectively. (d) Histogram of pick differences relative to the time average differences between FZHW and DWSAs.

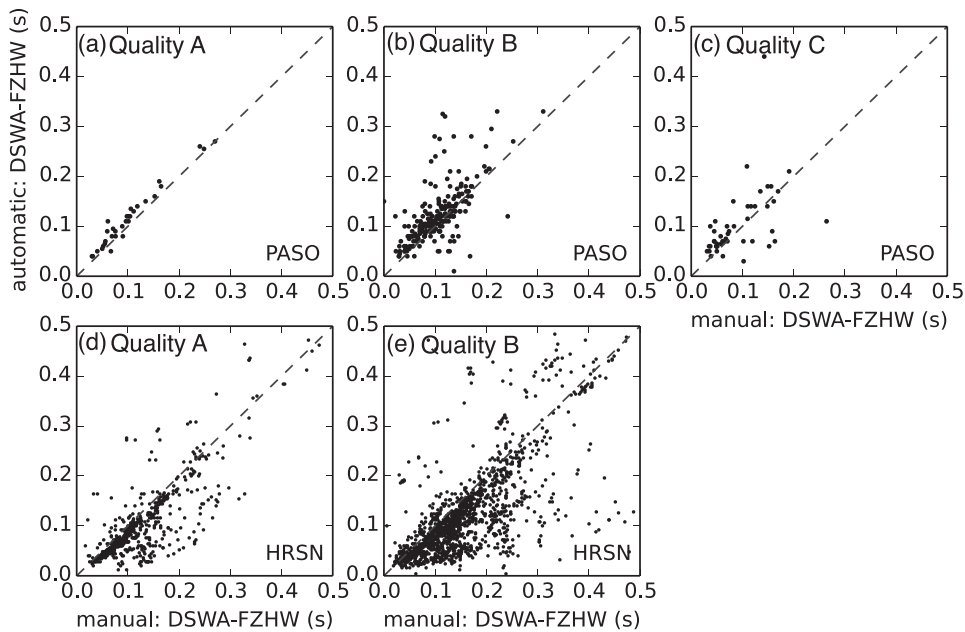


Figure 6. (a–c) Comparison of picks with different quality (A–C) and manual picks on the PASO network. (d–e) Same comparison on the HRSN network (qualities A and B).

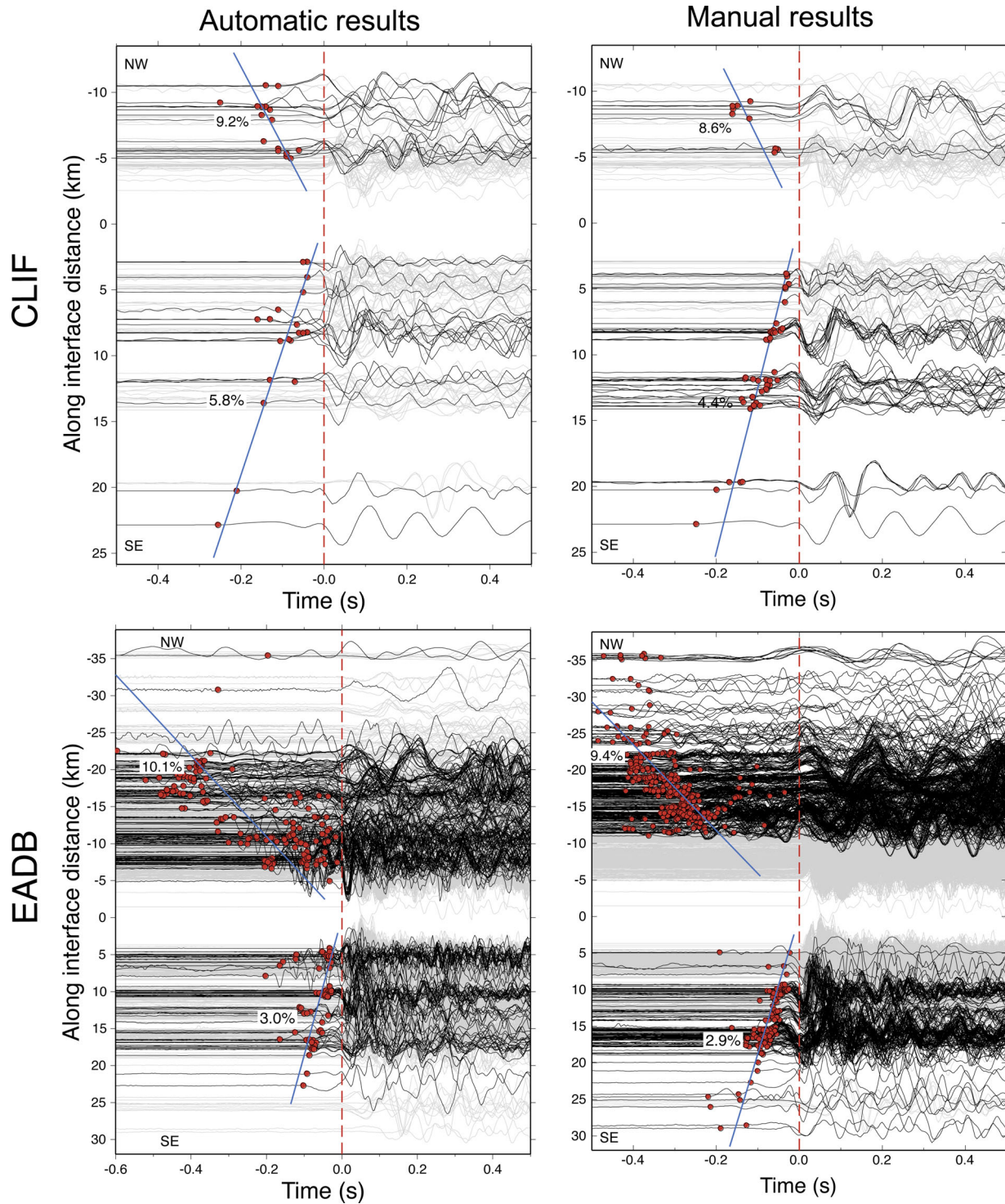


Figure 7. Comparison of automatically and manually picked DWSA at the PASO station CLIF and the HRSN station EADB. (a) Velocity seismograms recorded at the PASO station CLIF showing the moveout between FZHW and DWSA picked automatically (left) and manually (right). Black ones are waveforms with FZHW and grey ones are only with direct *P* waves. The red dots are the FZHW arrivals and the waveforms are aligned at the picked DWSA (red dash line). The blue lines are the linear regression without intercept term. The corresponding velocity contrast estimated from the slope is labelled. (b) Comparison on the HRSN station EADB. Symbols are the same as in panel (a).

Figs 8(a)–(c) show additional examples of FZHWs at stations CVCR, MMNB and PGH that are located on the NE (slow) side from NW to SE along the SAF (Fig. 2). They record substantial FZHWs and show systematic moveout between FZHWs and DWSAs. In comparison, the stations on the SW (fast) side have

very few FZHWs, and do not have clear systematic moveout with along-strike distances (e.g. SMNB, Fig. 8d).

We summarize the obtained velocity contrasts for sections to the NW and SE centred at the stations in the Parkfield area (Fig. 9a). A general pattern is that the velocity contrast is high near the Middle

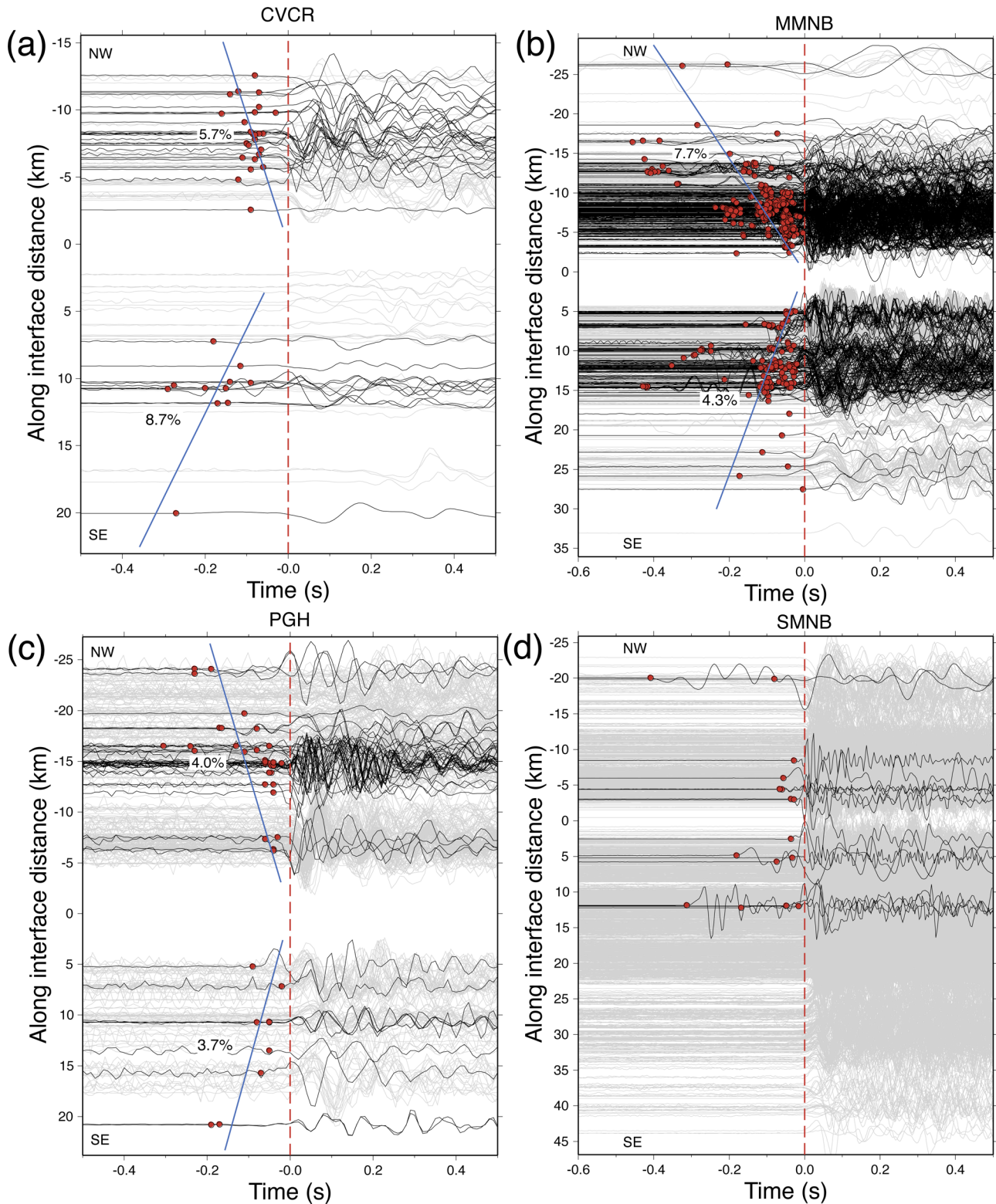


Figure 8. Examples of velocity seismograms showing the FZHW and automatically picked DWSA arrivals (see station locations in Fig. 2). (a–c) velocity seismograms recorded at the PASO station CVCR, the HRSN station EADB, the NCSN station PGH, respectively. Among them, CVCR is considered to be within the FZ group, and the other two are on the NE side. (d) velocity seismograms recorded at HRSN station SMNB on the SW side showing sparse FZHW and random moveout between FZHW and DWSA. Other symbols are the same as Fig. 7.

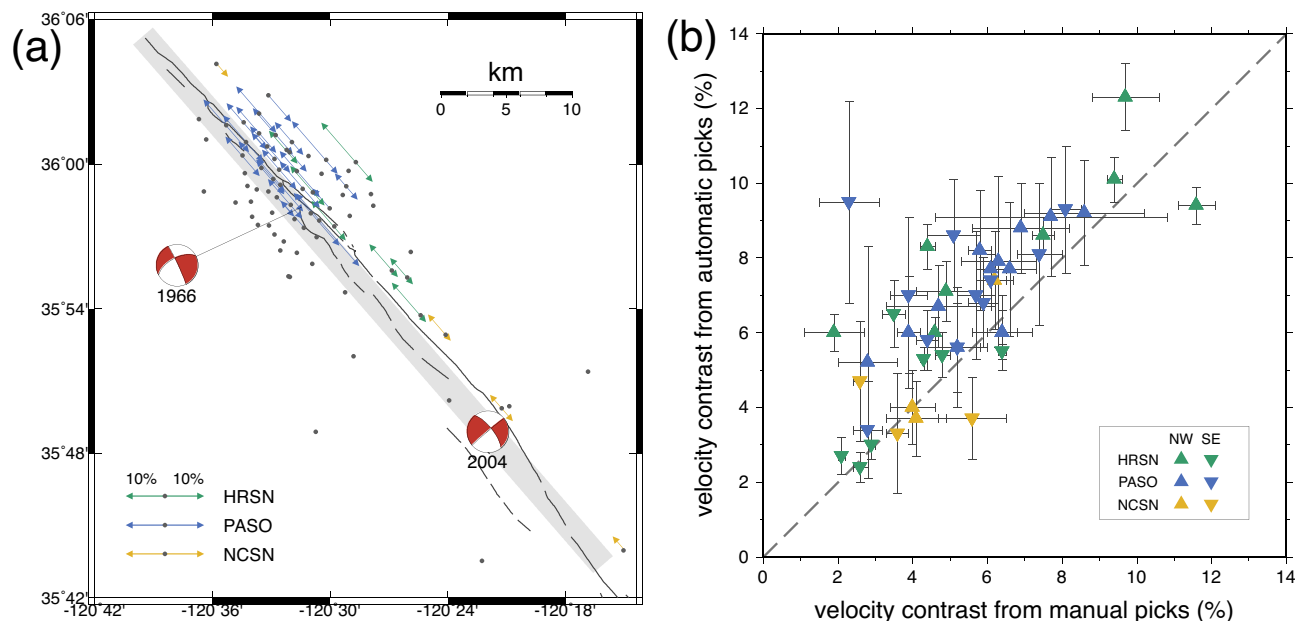


Figure 9. A summary of the obtained velocity contrasts across the Parkfield section of the SAF. Arrow length represents the velocity contrast value, and arrow direction represents the obtained velocity contrast using events from either NW or SE direction. Blue dots are stations. Other symbols are the same as in Fig. 1. (b) Comparison of velocity contrasts measured from automatically and manually picked DWSAs. Blue, green and yellow symbols represent results for the PASO, HRSN and NCSN network, respectively. Triangles and inverse triangles are measurements using events from NW and SE directions, respectively. The dashed line marks the one to one relationship. Horizontal and vertical error bars are for manual and automatic results, respectively.

Mountain and diminishes towards Gold Hill. The velocity contrast is below 5 per cent near the epicentre of the 2004 Parkfield earthquake. This is consistent with Zhao *et al.* (2010), although we have 11 more stations in the FZ group. A direct comparison of the velocity contrasts between the automatic and manual picks shows that they generally follow the 1-1 line, despite a few outliers (9b). Nevertheless, the velocity contrasts to the NW tend to have high values (5–10 per cent), while the velocity contrasts to the SE are significantly clustered at the low values (<5 per cent).

4.3 False detection and misidentification of FZHWs

It is possible that some early arrivals other than FZHWs may share some common features with FZHWs, which may be caused by site effect, surface reflection, horizontal interfaces, and/or source effects. Our method and quality control scheme is designed to look for phases that have consistent FZHW characteristics, which is expected to reduce the picks of phases induced by other effects. However, false picks are still inevitable due to waveform complexity. Therefore, it is important to check the rate of false picks, in order to properly evaluate the effectiveness of our automatic method. FROB station is of particular interest because it is on the SW side but has 18.7 per cent FZHW detection rate. One possible explanation is that these FZHWs are produced by a local reversal of velocity contrast (Fig. 10b) between Middle Mountain and Gold Hill that was imaged by *P*-wave and joint *P*-FZHW tomography (Thurber *et al.* 2006; Bennington *et al.* 2013). However, most picks on FROB show no clear systematic moveout with increasing along-fault interface distance (Fig. 10b). Given that FZHWs should have reverse polarity predicted by the focal mechanism, we inspect some of the detections and indeed find a significant portion of dubious picks, as shown in Fig. 11. The waveforms of these early arrivals all have weak amplitudes, which is one of the important characteristics of

FZHW. However, a systematic inspection of waveforms on FROB reveals that 94 per cent of the identified ‘FZHW’ phases have first motion consistent with the predictions for the direct *P* waves with right-lateral strike-slip radiation patterns, which is inconsistent with opposite polarity of FZHW and direct *P* wave associated with a shear slip on the bi-material interface. A similar result is observed on SMNB. One possible explanation could be that FZHW and direct *P* wave take off in the same quadrant, resulting in similar polarity. In other words, their focal mechanisms are not purely strike-slip on the SAF. However, this phenomenon is only observed at a few stations on the SW side. For example, for MMNB and EADB, we find only a 5–10 per cent of identifications are suspicious (i.e. same polarities between the *P* and FZHWs). These observations are also consistent with the systematic moveout observed at stations EADB and MMNB, and lack of moveout at stations FROB and SMNB. For now we tentatively classify those observed at stations FROB and SMNB as ‘false picks’. A detailed study is needed to further identify the cause of these weak amplitude phases at stations on the SW side of the SAF.

In addition to ‘false picks’, the method also missed some picks present in manual results. This could be due to the requirement of mutual agreement between LAAR and SAAR picks, which is meant to minimize the number of false picks rather maximize detection rate. Besides, manual inspection has flexibility to adjust and reconsider the picks based on the general profiles and moveout (Allam *et al.* 2014), while the automatic method follows more objective criteria without human interference. Another piece of uncertainty results from possible multiple phases present in the search window. In this case, the LAAR and SAAR curves may have different maxima (Supporting Information Fig. S2), and hence is either dropped out or flagged with low qualities. But this issue is also not avoidable for manual picking. It inherently lies in the difficulty in recognizing the real ray path for multiple phases using a single waveform.

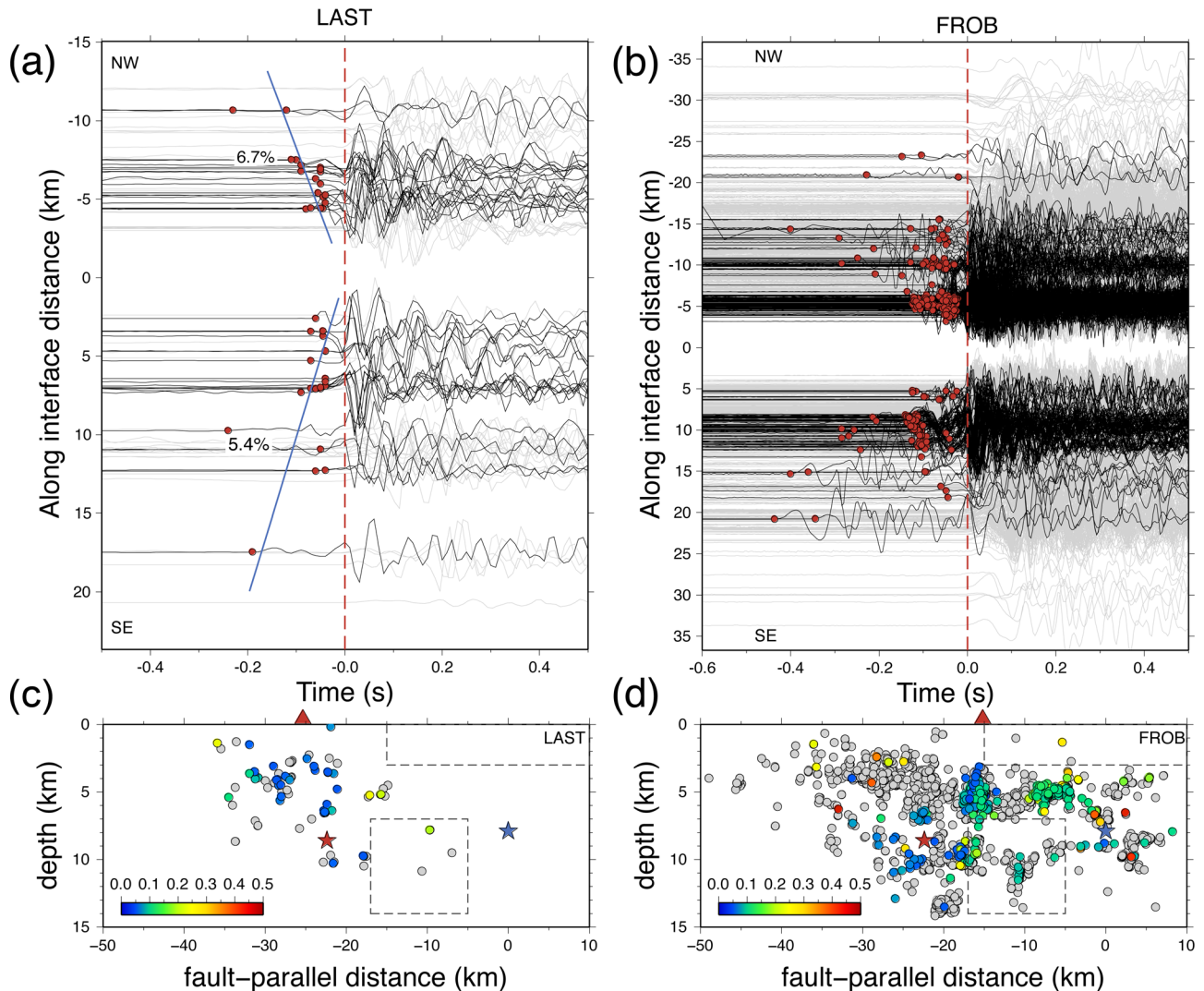


Figure 10. Examples of FZHWs and/or FZHW-like signals recorded by the FZ station LAST and station FROB in the SW side (see station locations in Fig. 2). (a) Moveout of FZHWs with along-strike distances at FZ station LAST. The bottom panel shows the cross-section of events with and without FZHW generation. The events with FZHWs are coloured by the time differences between the DWSA and FZHW arrivals. Grey background dots represent events without FZHWs. Red triangle marks the station. The red and blue stars mark the epicentres of the 1966 and 2004 M6-type Parkfield earthquakes, respectively. Dashed boxes mark the approximated location of reverse velocity contrast patches observed by Thurber *et al.* (2006). (b) Moveout of FZHWs (top) and cross-section of events recorded at station FROB in the SW side. Other symbols are the same as in panel (a).

5 DISCUSSIONS

In this study, we presented an automatic method to detect FZHWs and DWSAs, which allowed us to systematically re-analyse bimaterial fault properties in the Parkfield of the SAF. The obtained velocity contrast shows clear along fault-strike variations, which agreed well with the results from manual picks (Zhao *et al.* 2010). The overall patterns of velocity contrast are also compatible with both geological and geophysical observations that the NE block has slower velocity than the SW block (e.g. Eberhart-Phillips & Michel 1993; Thurber *et al.* 2006).

One notable difference is that our automatic search method identifies a large number of FZHWs at FZ stations, which has not been reported by Zhao *et al.* (2010). For example, we found 45.5 per cent FZHW rate on the LAST station, while Zhao *et al.* (2010) did not report any FZHW on this station at all (Fig. 3). The FZ stations have comparable percentage of FZHW observations with the stations on the NW side and also show systematic moveout (e.g. station LAST,

Fig. 10a). The velocity contrasts at FZ stations are comparable those at stations on the NW side (Fig. 12). Note that our approximated fault line mainly follow the aftershocks of the 2004 Parkfield event, which is close to the surface expression of the South West Fracture Zone (SWFZ), rather than the main trace of the SAF (Thurber *et al.* 2006). In this case, our observations contradict a fault model that is simply composed of a fast and slow block on both sides of the fault interface (e.g. Ben-Zion & Malin 1991; Zhao *et al.* 2010).

Instead, our observation could be qualitatively explained by a wide low-velocity zone (LVZ) sandwiched between two quarter-spaces (Fig. 12). In this case, the LVZ would produce two velocity contrast interfaces against two blocks, resulting in FZHWs observed at most stations within the LVZ. At Parkfield, features of LVZ have been observed, based on fault zone trapped waves (FZTW) that propagate within a narrow LVZ (Li *et al.* 2004; Lewis & Ben-Zion 2010), as well as wider zones at regional scale from traveltime inversions (e.g. Zhang *et al.* 2009), attenuation (Bennington *et al.*

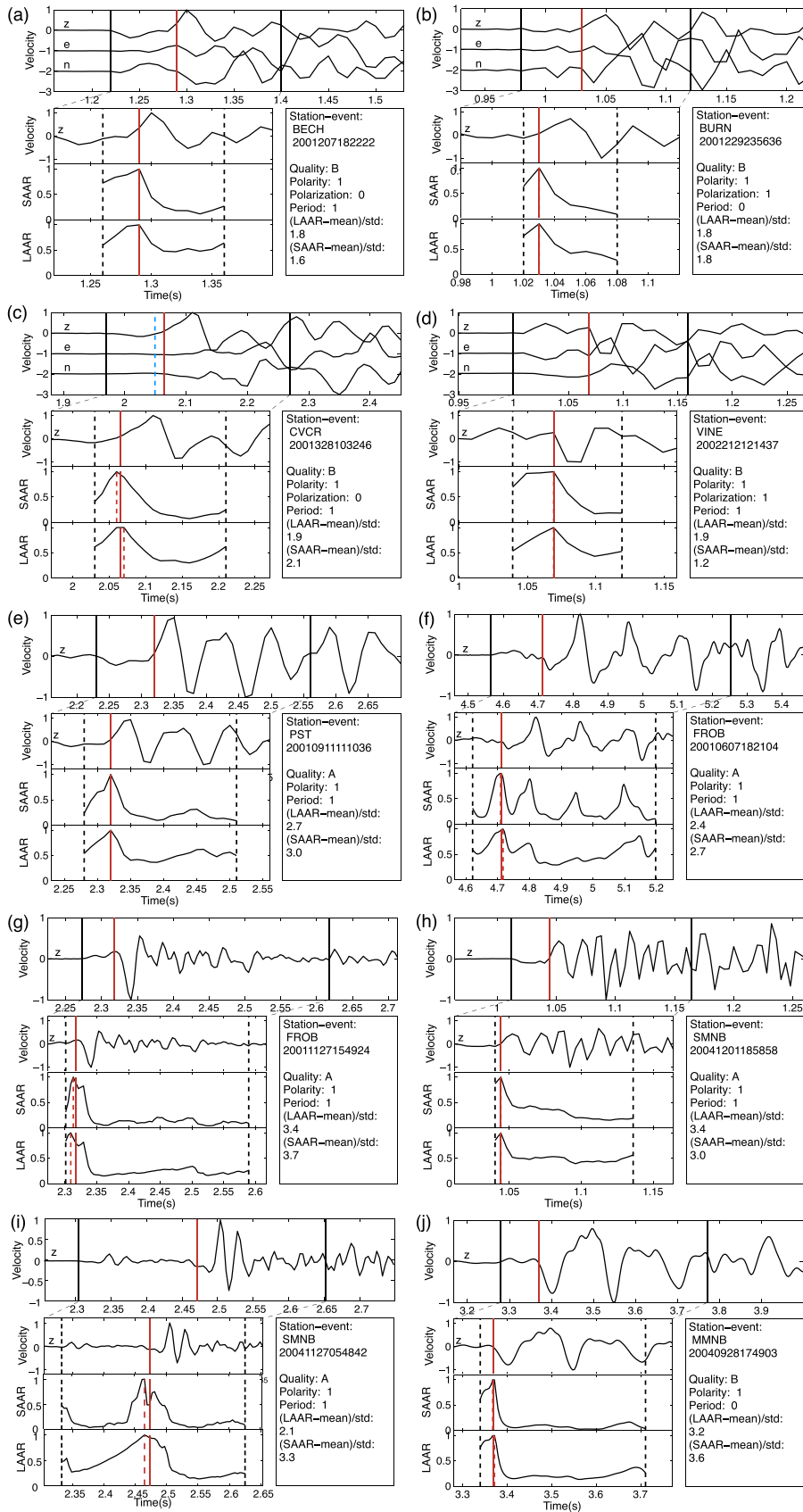


Figure 11. Examples of false detections of FZHW. Symbols are the same as in Fig. 4.

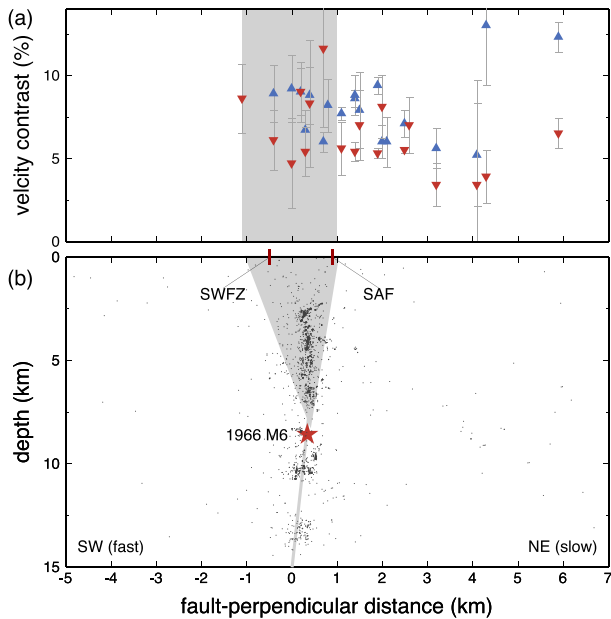


Figure 12. (a) Velocity contrast values across the fault around the 1966 M6 epicentre. Blue triangles and red inverse triangles are measurements using events from NW and SE sides of the stations, respectively. (b) A schematic fault model. The grey area represents the approximate location of the low velocity damage zone and the primary fault interface. The red triangles mark the surface expression of the Southwest Fracture Zone (SWFZ) and the main trace of the San Andreas Fault (SAF). The red star represents the hypocentre of the 1966 M6 earthquake. The background seismicities are events in 1984–2006 within 5 km from the 1966 M6 epicentre along the fault strike (Thurber *et al.* 2006).

2008), and magnetotelluric observations (Unsworth & Bedrosian 2004). The width of LVZ inferred from FZTWs are generally 200–300 m, while the width from other studies are generally on the order of 1–2 km, bounded by the SWFZ and the main trace of the SAF. This suggests that large major fault zones like the SAF likely have hierarchical structures (e.g. Ben-Zion & Sammis 2003) so that large-scale LVZs can be detected only by the regional-scale geophysical inversions, while FZTW observations have higher resolution but are based on short cross-fault arrays (a few hundred meters) and hence are able to see at finer-scale local FZ structures. It is also possible is that regional-scale geophysical inversions do not have the resolution to image the few-hundred-meter wide trapping structures, while the dense cross-fault arrays are not long enough to reveal the 1–2 km wide less-damaged FZ structures (e.g. Cochran *et al.* 2009).

Nevertheless, our observation of FZHWs for stations on both sides of FZs is generally consistent with the existence of a wider LVZ at Parkfield. Interestingly, Yang *et al.* (2015) also found clear FZHWs on both sides of the faults that ruptured during the 2010 M_w 6.9 Yushu earthquake sequence, and they suggested an existence of a 5-km wide LVZ beneath a pull-apart basin. Simulations of in-plane rupture show that, in such type of sandwich structure, rupture tends to migrate spontaneously to both bimaterial interfaces, with each interface having opposite preferred propagation direction (Brietzke & Ben-Zion 2006).

Horizontal polarization has been used to distinguish FZHW and DWSA (Bulut *et al.* 2012; Allam *et al.* 2014; Yang *et al.* 2015), because DWSA is expected to be radial while FZHW is radiated from the fault with a certain angle to the radial direction. We include this in our algorithm as a quality factor (eq. 8). However, it is somewhat

surprising that only 56.4 per cent automatic measurements meet this requirement, which is barely above the 50-50 per cent chance. This is not only observed in the automatic results, but also in the manual picks from Zhao *et al.* (2010), whose value is 53.1 per cent. Fig. 13 shows the polarization angles of FZHWs and DWSAs against the event back azimuths, and the difference between them. We do not observe clear deviation of FZHW polarizations from back azimuths. Instead, they have large scatters similar to these of DWSAs. Again, this also occurs to the manual case (Supporting Information Fig. S3).

Several possible factors may account for these observations. First, the amplitudes of FZHW and direct P waves on horizontal components are relatively low. Hence they are likely contaminated by the pre-event noises. Second, assuming 10 per cent average velocity contrast, the difference of polarization angles of FZHW and direct P waves is $\sim 30^\circ$ theoretically. When projected to horizontal plane, this angle could become even smaller. Such a difference may not be resolvable with the presence of noise and other complex phases. Third, fault zones are strongly heterogeneous and the structures are usually complicated than a two half spaces or sandwiched fault zone model (e.g. Ben-Zion 1998). In addition, depending on the frequency content, polarizations of FZHW and direct P waves may be sensitive to local structural complexities rather than the average velocity contrasts.

While individual picks, seismic profiles and velocity contrast pattern between automatic and manual results show general agreements, there are several notable issues that are worth discussing further. First, in the algorithm we used one average period T_d following the initial pick to check whether the first phase is sharp or not. This in fact sets a minimal value of velocity contrast that can be resolved by the technique. Therefore, the use of T_d may reduce the resolution of the method. The obtained average value of T_d in our data set is ~ 0.06 s (6 samples), which corresponds to a minimal step of velocity contrast of 1–3 per cent, depending on the P wave traveltime. However, in practice it is always difficult to distinguish two phases if they are a few centiseconds apart. Ross & Ben-Zion (2014) also set a minimum allowed time difference between the initial and second pick to be 0.065 s in order to approximate the length of two wiggles of a direct P wave. Decreasing this value would increase the resolution of smaller velocity contrast but may introduce more false picks.

In addition to Parkfield, we also applied it in the Yushu region in northern Tibet following the 2010 M_w 6.9 Yushu earthquake, and we found general agreement between manual and automatic picks (fig. S6 in Yang *et al.* 2015). Therefore, we expect our method can be applied to identify FZHWs in large local earthquake data set with one or three component recordings. While in present FZHWs have been identified only in vertical strike-slip environment, it can be also applied to thrust or other tectonic environments (e.g. Fukao *et al.* 1983).

Finally we list a few parameters that need be treated with precaution in the application of other regions. First, T_d is calculated using the waveform within the search window. However, to avoid unfeasibly large value of T_d , it is useful to set an upper limit (e.g. 0.08–0.1 s), depending somewhat on the sampling rate and dominant frequency content of the actual data. Second, the maximum allowed velocity contrast K_{\max} also needs to be modified. In Parkfield, we use 15 per cent based on previous observations. But this value could be different in other regions. One should note that a higher threshold might lead to detection of other phases that arrives at later times. If the priori estimate is unavailable, we recommend setting a relatively high value (e.g. 20 per cent) in the initial stage.

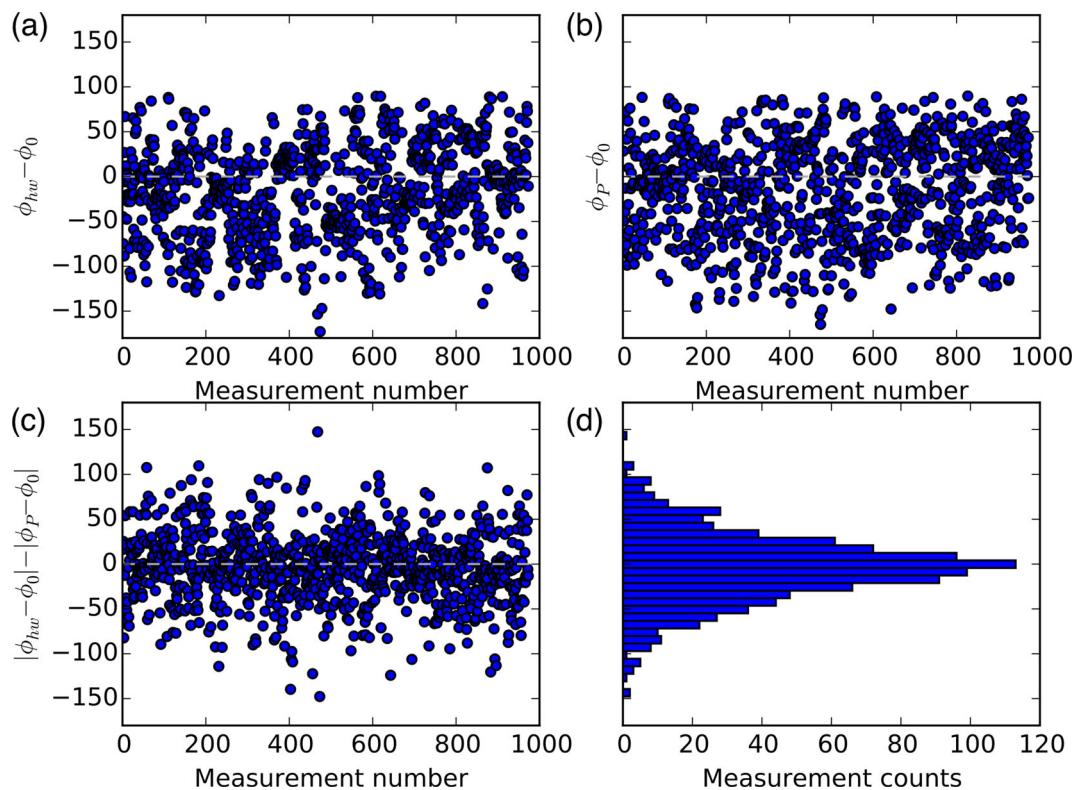


Figure 13. Statistical analysis of FZHW and DWSA polarization using automatic picks. (a) Polarization angle difference between FZHW and back azimuths for all measurements. (b) Polarization angle difference between DWSA and back azimuths for all measurements. (c) Comparison of deviation from back azimuth between FZHW and DWSA (see also eq. 8). (d) Histogram of panel (c).

After obtaining the preliminary DWSA picks, one can estimate the velocity contrast for each single measurement using eq. (1). By checking the overall velocity contrast values, a proper value of K_{\max} can be set to exclude outliers or other phases in the second run. As shown in Supporting Information Fig. S4, the inaccuracy of first arrival picks will affect the DWSA picks and also lead to erroneous estimate of velocity contrast. This requires the input first arrivals to have relatively high quality. Hence, it is recommended to check the accuracy of first arrival picks whether they are from manual or automatic methods.

ACKNOWLEDGEMENTS

We thank Editor Eiichi Fukuyama, Editor Yehuda Ben-Zion, reviewer Fatih Bulut and another anonymous reviewer for the constructive comments. The waveform data of the High Resolution Seismic Network operated by the Berkeley Seismological Laboratory, University of California, Berkeley, and the Northern California Seismic Center operated by the U.S. Geological Survey, Menlo Park, can be obtained from the Northern California Earthquake Data Center (NCEDC). We thank Professor Haijiang Zhang for providing the Parkfield Area Seismic Observatory (PASO) data used in this and in Zhao *et al.* (2010). The manuscript benefits from useful comments/discussions with Zachary Ross. This study was supported by NSF grant EAR-0908310 and EAR-1447091.

REFERENCES

Allam, A.A., Ben-Zion, Y. & Peng, Z., 2014. Seismic imaging of a bimaterial interface along the Hayward fault, CA, with fault zone head waves and direct P arrivals, *Pure appl. Geophys.*, **171**, doi:10.1007/s00024-014-0784-0.

- Ampuero, J.P. & Ben-Zion, Y., 2008. Cracks, pulses and macroscopic asymmetry of dynamic rupture on a bimaterial interface with velocity-weakening friction, *Geophys. J. Int.*, **173**, 674–692.
- Andrews, D.J. & Ben-Zion, Y., 1997. Wrinkle-like slip pulse on a fault between different materials, *J. geophys. Res.*, **102**, 553–571.
- Barnes, A.E., 1993. Instantaneous spectral bandwidth and dominant frequency with applications to seismic reflection data, *Geophysics*, **58**, 419–428.
- Bennington, N., Thurber, C. & Roecker, S., 2008. Three-dimensional seismic attenuation structure around the SAFOD site, Parkfield, California, *Bull. seism. Soc. Am.*, **98**(6), 2934–2947.
- Bennington, N.L., Thurber, C., Peng, Z.G., Zhang, H.J. & Zhao, P., 2013. Incorporating fault zone head wave and direct wave secondary arrival times into seismic tomography: application at Parkfield, California, *J. geophys. Res.*, **118**(3), 1008–1014.
- Ben-Zion, Y., 1989. The response of two joined quarter spaces to SH line sources located at the material discontinuity interface, *Geophys. J. Int.*, **98**, 213–222.
- Ben-Zion, Y., 1990. The response of two half spaces to point dislocations at the material interface, *Geophys. J. Int.*, **101**, 507–528.
- Ben-Zion, Y., 1998. Properties of seismic fault zone waves and their utility for imaging low velocity structures, *J. geophys. Res.*, **103**, 12 567–12 585.
- Ben-Zion, Y., 2001. Dynamic ruptures in recent models of earthquake faults, *J. Mech. Phys. Solids*, **49**, 2209–2244.
- Ben-Zion, Y., 2006. Comment on “material contrast does not predict earthquake rupture propagation direction” by R.A. Harris and S.M. Day, *Geophys. Res. Lett.*, **33**(13), doi:10.1029/2005gl025652.
- Ben-Zion, Y. & Malin, P., 1991. San-Andreas fault zone head waves near Parkfield, California, *Science*, **251**, 1592–1594.
- Ben-Zion, Y. & Sammis, C.G., 2003. Characterization of fault zones, *Pure appl. Geophys.*, **160**, 677–715.
- Ben-Zion, Y., Katz, S. & Leary, P., 1992. Joint inversion of fault zone head waves and direct-P arrivals for crustal structure near major faults, *J. geophys. Res.*, **97**, 1943–1951.

- Brietzke, G.B. & Ben-Zion, Y., 2006. Examining tendencies of in-plane rupture to migrate to material interfaces, *Geophys. J. Int.*, **167**, 807–819.
- Brietzke, G.B., Cochard, A. & Igel, H., 2009. Importance of biomaterial interfaces for earthquake dynamics and strong ground motion, *Geophys. J. Int.*, **178**(2), 921–938.
- Bulut, F., Ben-Zion, Y. & Bohnhoff, M., 2012. Evidence for a bimaterial interface along the Mudurnu segment of the North Anatolian fault zone from polarization analysis of *P* waves, *Earth planet. Sci. Lett.*, **327**, 17–22.
- Cochran, E.S., Li, Y.G., Shearer, P.M., Barbot, S., Fialko, Y. & Vidale, J.E., 2009. Seismic and geodetic evidence for extensive, long-lived fault damage zones, *Geology*, **37**, 315–318.
- Dalguer, L.A. & Day, S.M., 2007. Staggered-grid split-node method for spontaneous rupture simulation, *J. geophys. Res.*, **112**, doi:10.1029/2006JB004467.
- Dalguer, L.A. & Day, S.M., 2009. Asymmetric rupture of large aspect-ratio faults at bimaterial interface in 3D, *Geophys. Res. Lett.*, **36**, L23307, doi:10.1029/2009GL040303.
- Dor, O., Yildirim, C., Rockwell, T.K., Ben-Zion, Y., Emre, O., Sisk, M. & Duman, T.Y., 2008. Geological and geomorphologic asymmetry across the rupture zones of the 1943 and 1944 earthquakes on the North Anatolian fault: possible signals for preferred earthquake propagation direction, *Geophys. J. Int.*, **173**(2), 483–504.
- Eberhart-Phillips, D. & Michel, A.J., 1993. Three-dimensional velocity structure, seismicity, and fault structure in the Parkfield region, central California, *J. geophys. Res.*, **98**, 15 737–15 758.
- Fukao, Y., Hori, S. & Ukawa, M., 1983. A seismological constraint on the depth of the basalt-eclogite transition in a subducting oceanic crust, *Nature*, **303**, 413–415.
- Jurkevic, A., 1988. Polarization analysis of three-component array data, *Bull. seism. Soc. Am.*, **78**, 871–884.
- Lewis, M.A. & Ben-Zion, Y., 2010. Diversity of fault zone damage and trapping structures in the Parkfield section of the San Andreas fault from comprehensive analysis of near fault seismograms, *Geophys. J. Int.*, **183**(3), 1579–1595.
- Li, Y.G., Vidale, J.E. & Cochran, E.S., 2004. Low-velocity damaged structure of the San Andreas fault at Parkfield from fault zone trapped waves, *Geophys. Res. Lett.*, **31**(12), doi:10.1029/2003gl019044.
- McGuire, J. & Ben-Zion, Y., 2005. High-resolution imaging of the bear valley section of the San Andreas fault at seismogenic depths with fault-zone head waves and relocated seismicity, *Geophys. J. Int.*, **163**, 152–164.
- Peng, Z., Long, L.T. & Zhao, P., 2011. The relevance of high-frequency analysis artifacts to remote triggering, *Seismol. Res. Lett.*, **82**(5), 654–660.
- Ross, Z.E. & Ben-Zion, Y., 2014. Automatic picking of direct *P*, *S* seismic phases and fault zone head waves, *Geophys. J. Int.*, **199**, 368–381.
- Shi, Z.Q. & Ben-Zion, Y., 2006. Dynamic rupture on a bimaterial interface governed by slip-weakening friction, *Geophys. J. Int.*, **165**, 469–484.
- Thurber, C., Zhang, H.J., Waldhauser, F., Hardebeck, J., Michael, A. & Eberhart-Phillips, D., 2006. Three-dimensional compressional wavespeed model, earthquake relocations, and focal mechanisms for the Parkfield, California region, *Bull. seism. Soc. Am.*, **96**, S38–S49.
- Unsworth, M. & Bedrosian, P.A., 2004. Electrical resistivity structure at the SAFOD site from magnetotelluric exploration, *Geophys. Res. Lett.*, **31**(12), doi:10.1029/2003gl019405.
- Wdowinski, S., Smith-Konter, B., Bock, Y. & Sandwell, D., 2007. Diffuse interseismic deformation across the Pacific-North America plate boundary, *Geology*, **35**, 311–314.
- Weertman, J., 1980. Unstable slippage across a fault that separates elastic media of different elastic constants, *J. geophys. Res.*, **85**, 1455–1461.
- Xu, S., Ben-Zion, Y. & Ampuero, J.-P., 2012. Properties of inelastic yielding zones generated by in-plane dynamic ruptures: II. Detailed parameter-space study, *Geophys. J. Int.*, **191**, 1343–1360.
- Yang, W., Peng, Z., Wang, B., Li, Z. & Yuan, S., 2015. Velocity contrast along the rupture zone of the 2010 M_w 6.9 Yushu, China earthquake from fault zone head waves, *Earth planet. Sci. Lett.*, **416**, 91–97.
- Zhang, H.J., Thurber, C. & Bedrosian, P., 2009. Joint inversion for V_p , V_s , and V_p/V_s at SAFOD, Parkfield, California, *Geochem. Geophys. Geosyst.*, **10**, doi:10.1029/2009gc002709.
- Zhao, P., Peng, Z.G., Shi, Z.Q., Lewis, M.A. & Ben-Zion, Y., 2010. Variations of the velocity contrast and rupture properties of M_6 earthquakes along the Parkfield section of the San Andreas fault, *Geophys. J. Int.*, **180**, 765–780.

SUPPORTING INFORMATION

Additional Supporting Information may be found in the online version of this paper:

Figure S1. Comparison of pick examples without (a) and with (b) the modulation term $R(t)$ in LAAR and SAAR. Symbols are the same as Fig. 4. It can be seen that the without $R(t)$, the curves of LAAR and SAAR show an erroneous pick at the first arrival since the existing ‘first arrival’ pick is incorrect.

Figure S2. Examples of multiple phases that exist in the early portion of the waveform, which can be seen in multiple peaks of the LAAR and SAAR curves. Symbols are the same as Fig. 4.

Figure S3. Statistical analysis of FZHW and DWSA polarization using manual picks from Zhao *et al.* (2010). (a) Polarization angle difference between FZHW and back azimuths for all measurements. (b) Polarization angle difference between DWSA and back azimuths for all measurements. (c) Comparison of deviation from back azimuth between FZHW and DWSA (see also eq. 8). (d) Histogram of panel (c).

Figure S4. Examples of erroneous picks that may occur when the initial pick is incorrect. Symbols are the same as Fig. 4 (<http://gji.oxfordjournals.org/lookup/suppl/doi:10.1093/gji/ggw082/-/DC1>).

Please note: Oxford University Press is not responsible for the content or functionality of any supporting materials supplied by the authors. Any queries (other than missing material) should be directed to the corresponding author for the paper.